Meteoritics & Planetary Science 39, Nr 3, 467–479 (2004)
Abstract available online at http://meteoritics.org

Ejecta formation and crater development of the Mjølnir impact

Valery SHUVALOV[1*] and Henning DYPVIK[2]

[1*]Institute of Geosphere Dynamics, Russian Academy of Sciences, 38 Leninsky Prospect, Building 1, 119334, Moscow, Russia
[2]Department of Geosciences, University of Oslo, Post Office Box 1047, Blindern, N-0316, Norway
[*]Corresponding author. E-mail: shuvalov@idg.chph.ras.ru

(Received 14 February 2003; revision accepted 16 January 2004)

Abstract–Crater-ejecta correlation is an important element in the analysis of crater formation and its influence on the geological evolution. In this study, both the ejecta distribution and the internal crater development of the Jurassic/Cretaceous Mjølnir crater (40 km in diameter; located in the Barents Sea) are investigated through numerical simulations. The simulations show a highly asymmetrical ejecta distribution, and underscore the importance of a layer of surface water in ejecta distribution. As expected, the ejecta asymmetry increases as the angle of impact decreases. The simulation also displays an uneven aerial distribution of ejecta.

The generation of the central high is a crucial part of crater formation. In this study, peak generation is shown to have a skewed development, from approximately 50–90 sec after impact, when the peak reaches its maximum height of 1–1.5 km. During this stage, the peak crest is moved about 5 km from an uprange to a downrange position, ending with a final central position which has a symmetrical appearance that contrasts with its asymmetrical development.

INTRODUCTION

The Mjølnir submarine crater is a 40-km in diameter structure, located in the Barents Sea (Fig. 1). It is presently covered by 350 m of water and 50–400 m of younger sedimentary strata (Dypvik et al. 1996; Gudlaugsson 1993). Morphologically, the crater has the shape of an "inverted sombrero," with an 8 km-wide inner zone and a 12 km-wide outer zone (Fig. 2). The crater has a prominent central high, which protrudes 250 m above the crater floor (Tsikalas et al. 1998a) and is 8 km wide at the base. The slightly upraised rim shows the presence of several terraces down into the crater, with possible resurge gullies cutting through them. The terraces are bordered by faults, and the outermost terrace has a rim wall about 70 m high (Gudlaugsson 1993; Tsikalas et al. 1998a; 1998b). The depth of the transient cavity was at least 4.5 km (Tsikalas et al. 1998a).

The Mjølnir crater is filled by a 1 km-thick breccia unit (Tsikalas et al. 1998a; 1998b) and is interpreted as formed by an impact of an asteroid 1.5–2 km in diameter (Tsikalas et al. 1998b; Dypvik and Attrep 1999) into a 200–400 m-deep epicontinental paleo-Barents Sea. Micropaleontological, palynological, and macropaleontological studies, supported by seismic correlation, indicate an early Berriasian age (Berriasiella jacobi zone) of the impact layer (Dypvik et al. 1996; Smelror et al. 2001). The target consisted of an unconsolidated sedimentary sequence of Devonian to Jurassic age, which was at least 6 km thick, overlying older, well-lithified sedimentary strata (Dypvik et al. 1996).

The sedimentary succession in a drillcore collected 30 km outside the crater consists of black and gray, partly laminated claystones, which contain only a single 19 cm-thick conglomerate (Dypvik et al. 1996). Clay clasts are found at the base of this conglomerate, and shock-metamorphosed quartz grains are present throughout the conglomerate. This conglomerate most probably represents reworked fallout ejecta, which may have been modified by density currents, oscillating wave surges, or by a giant tsunami. Based on the occurrence of smectite and some other geochemical parameters, Dypvik and Ferrell (1998) and Dypvik and Attrep (1999) suggested that the original thickness of this impact-related bed was 3.2 m and that the 80 cm main ejecta layer formed its uppermost part. The lowermost 2.4 m of this succession is highly enriched in smectite (a clay-mineral alteration product of possible impact glass) compared to beds below and above (Dypvik and Ferrell 1998). This 3.2 m-thick ejecta succession is less than half of what is predicted by scaled ejecta blanket thickness estimation (according to Melosh 1989).

Iridium enrichments and Ni-rich, iron oxide grains found in correlative beds at the Svalbard Archipelago, about 400 km northwest of the Mjølnir Crater is considered to be strong

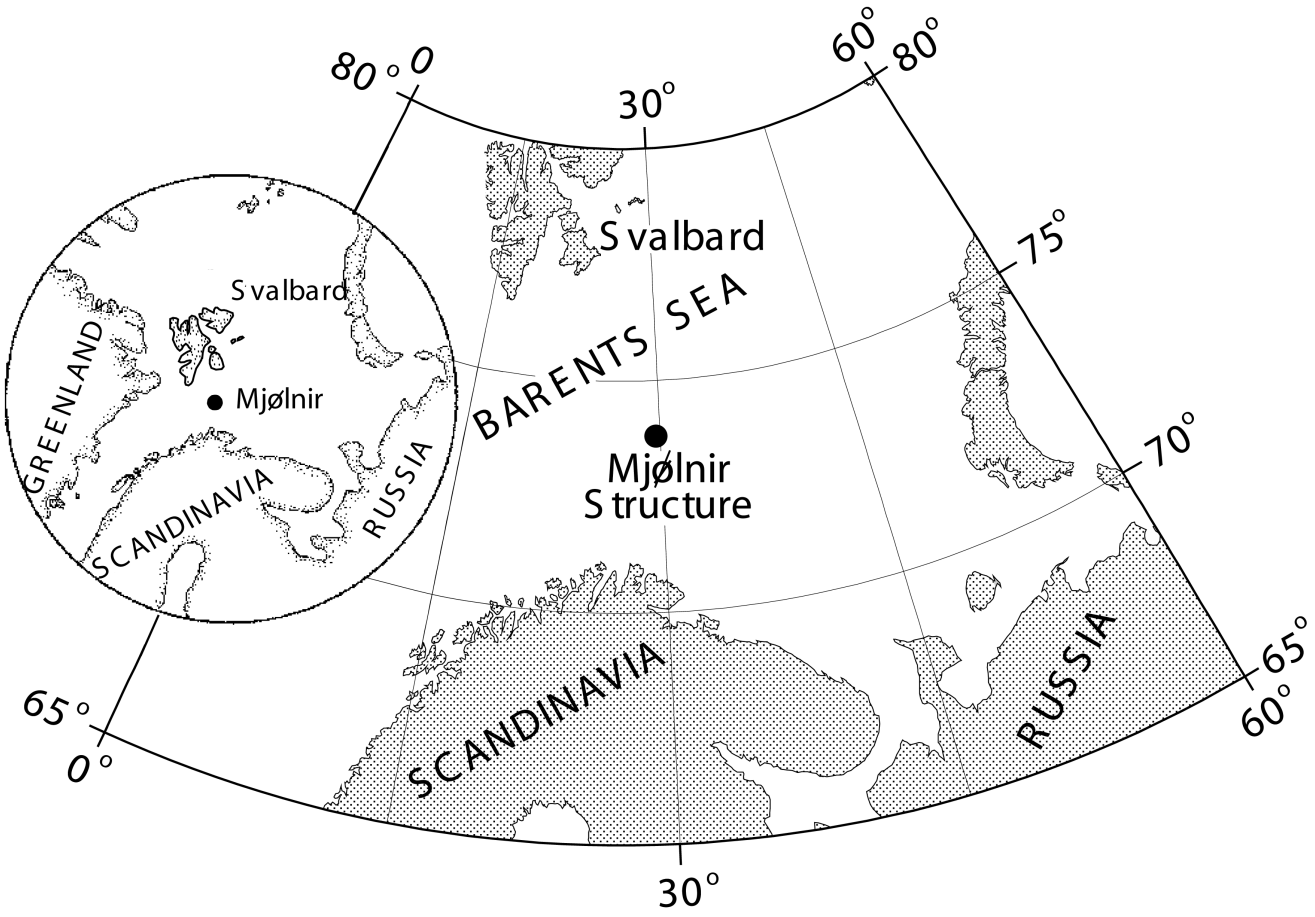

Fig. 1. Location map showing the Mjølnir structure. Modified from Dypvik and Ferrell (1998).

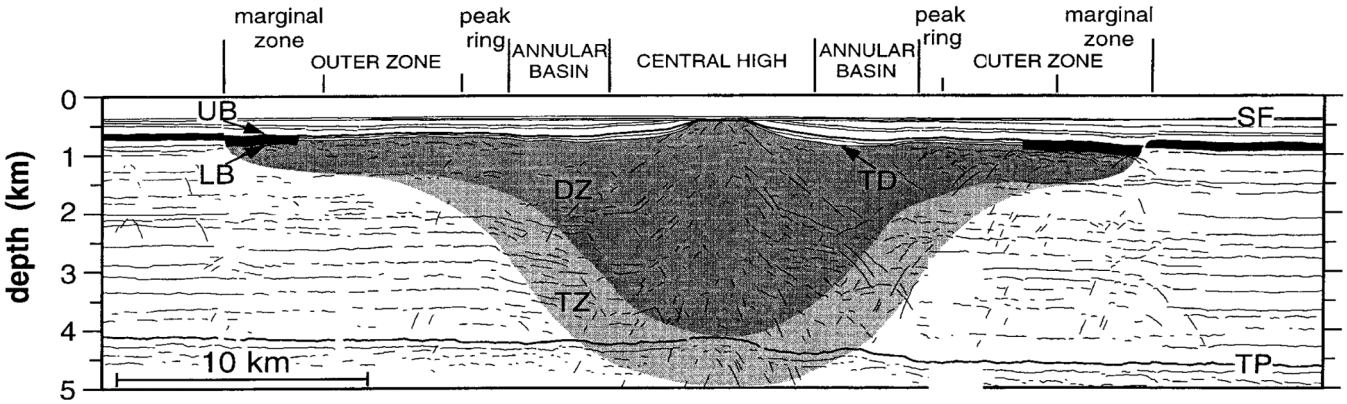

Fig. 2. The Mjølnir crater. Modified from Tsikalas (1998c).

evidence for impact ejecta (Robin et al. 2001; Kyte 2000, personal communication). Zakharov et al. (1993) found a very high Ir peak at the Jurassic–Cretaceous boundary (i.e., at the same stratigraphical level) in the Nordvik area of Siberia, which is currently located about 2500 km to the east of the Mjølnir impact site. Based on detailed stratigraphical correlations, we consider that this iridium anomaly could be the result of the Mjølnir impact (Smelror et al. 2001). The simulation of Shuvalov et al. (2002) modeled the formation of the Mjølnir crater, but the development of the central high evolution and the ejecta formation and distribution were not discussed in detail. In a case like Mjølnir, a crater buried beneath sediments and water in the Barents Sea, understanding the ejecta formation may be particularly important because possible widespread ejecta are the most easily accessible impact products to study.

MODELS AND RESULTS

Model of Ejecta Formation and Deposition

The 2D and 3D versions of the SOVA multi-material hydrocode (see Shuvalov 1999) was previously used to model the Mjølnir crater formation (Shuvalov et al. 2002). In this study, we use this hydrocode to model the initial stage of the Mjølnir impact. The SOVA simulation terminates at the end of the excavation stage, when ejection velocity falls below 100 m/s (approximately 5 sec after Mjølnir impact began). The flight and ultimate deposition of the ejecta have been calculated using ballistic approximation. This approach is not very exact because both laboratory experiments (Schultz and Gault 1982) and numerical simulations (Shuvalov 2002) show that atmospheric drag and interaction with impact-produced vapor significantly modify the ballistic paths of ejecta smaller than some critical size. Consequently, this modification leads to separation of ejecta fragments by size within the ejecta cone. However, the overall ejecta curtain moves approximately ballistically, because its bulk density considerably exceeds the ambient air density. Moreover, most of the distal ejecta trajectory paths occur at high altitudes, where atmospheric drag is small. Given these factors, the ballistic approximation allows us to describe the ejecta curtain evolution qualitatively and to estimate its distribution on the Earth's surface quantitatively. At the same time, it is important to remember that the ballistic approximation is crude for both the initial and final portions of the ejecta. The initial (and the fastest) ejecta mainly consisting of vapor, has very low bulk density, and, therefore, experiences a great atmospheric drag even at high altitudes. In contrast, the final low velocity ejecta forming the crater rim has a great bulk density. In that case, the ejecta fragments strongly interact (collide) with each other, and their motion can not be described by ballistic flight of separated particles.

To test the model, we performed numerical simulations of the Mjølnir ejecta distribution after a vertical impact (2D simulations). Different spatial resolution and time (t_p) of passage from the SOVA calculations to the ballistic approximation were applied in the simulations. The projectile was modeled as a spherical asteroid 800 m in radius made of granite, with an impact velocity of 20 km/s. The target was approximated by wet tuff overlain by a 400 m-thick water layer. The Tillotson equation-of-state (Tillotson 1962) for water and wet tuff and ANEOS equation-of-state (Thompson and Lauson 1972) for granite were applied to calculate the materials' thermodynamic parameters. To model material strength, the approach developed by Melosh and Ivanov (1999) and O'Keefe and Ahrens (1999) was used. It is based on the "rigid-plastic" model (Dienes and Walsh 1973). For fractured rocks (i.e., loose materials with finite cohesion), the yield strength was defined as (Lundborg 1968; Zamishlyaev and Evterev 1990):

$$Y = \min(Y_0 + kP, Y_{max}) \quad (1)$$

where Y_0 is the cohesion, k is the coefficient of dry friction, P is the pressure, and Y_{max} is the limiting yield strength of the material at high pressure. According to previous studies (Shuvalov et al. 2002), a target with very low strength ($k \approx 0.05$) for the upper 3 km of sedimentary rocks and gradual increase of the strength from 3 to 6 km before getting values typical for granitic rocks (Y_0 = 1 MPa, k = 0.8, Y_{max} = 3 GPa) at greater depth was considered appropriate. The suggested mechanism of acoustic fluidization (Melosh 1989) was also taken into account using the method described in (Ivanov and Turtle 2001).

In the first set of test runs, the water layer was neglected. Fig. 3 shows the results for two different spatial resolutions. In both cases, the initial cell sizes h_z and h_r (along the z- and r-axis) were 40 m (40 cells across projectile diameter). The cell size and the size of computational region were doubled when the blast wave reached the grid boundary. The doubling continued until the cell sizes h_z and h_r reached maximum values h_{zmax} and h_{rmax}. The results for h_{zmax} = 80 m, h_{rmax} = 160 m (this spatial resolution was used in most 2D and partially 3D simulations) and for h_{zmax} = 160 m, h_{rmax} = 320 m (this spatial resolution was used in some 3D simulations) are shown in Fig. 3. Of course, different values of h_{zmax} and h_{rmax} imply different numbers of grid cells (240 × 240 and 120 × 120). The results show that both simulations give similar ejecta blanket thickness at distances 50–600 km from the crater center.

The comparison of results applying different t_p (Fig. 4) allows to estimate the validity of the ballistic approximation,

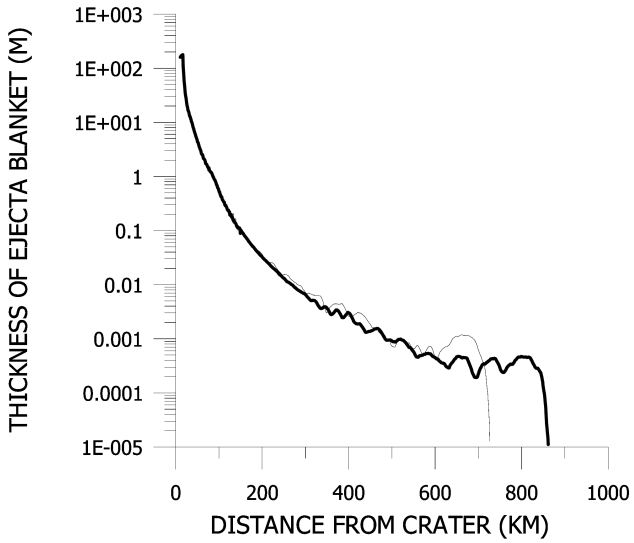

Fig. 3. Thickness of ejecta blanket versus distance from crater center obtained in calculations with t_p = 5 sec and different spatial resolution: h_{zmax} = 80 m, h_{rmax} = 160 m (thick gray line) and h_{zmax} = 160 m, h_{rmax} = 320 m (thin black line).

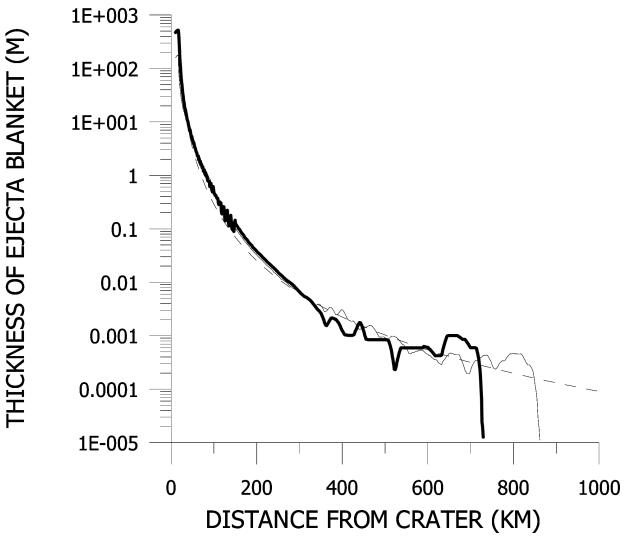

Fig. 4. Thickness of ejecta blanket versus distance from crater center obtained in calculations with h_{zmax} = 80 m, h_{rmax} = 160 m, and a different t_p: 5 sec (thin black line) and 20 sec (thick gray line). Dashed line shows an estimate from Equation 2.

because the SOVA simulations (used up to t_p) take atmospheric drag into account. The results correlate well at distances 50–600 km from the crater center. In the 3D simulations we used t_p = 5 sec.

Experimental data summarized by McGetchin et al. (1973) and Melosh (1989) give a thickness of ejecta blanket δ (for craters on land) in the form:

$$\delta = \alpha R(r/R)^{\beta}, \quad (2)$$

where *R* is a transient cavity radius (in m), *r* is a distance from crater center (in m), α = 0.04 (or some poorly known function of *R*), β = 3.0 ± 0.5. The dashed line in Fig. 4 shows an estimate of ejecta blanket thickness for the case under consideration resulting from Equation 2 assuming β = 3.5 and R = 12,000 m, the simulated transient crater radius for Mjølnir. The empirical curve correlate well with the results from numerical simulations at distances of 50–600 km from the crater center. At smaller distances a better correlation is obtained with β = 3.0.

Influence of Water Layer on the Ejecta Formation and Distribution

Numerical simulations of the Mjølnir impact showed (Shuvalov et al. 2002) that the 400-m water layer only slightly influenced the cratering process and the parameters of the final crater. Nevertheless, even such a shallow sea has a considerable influence on the formation and distribution of distal ejecta. Figure 5 demonstrates that the fastest (and, consequently, the farthest reaching) ejecta is ejected from the uppermost target layers. The figure shows part of the excavation process related to fast (>0.5 km/s) ejecta for an impact on land (upper panel) and an impact into 400 m-deep sea (lower panel). In these experiments, the ejection velocity was determined as the velocity t_p = 5 sec after the impact. Target rocks near the axis of symmetry were vaporized and ejected with high velocity, but experienced high atmospheric drag (due to low bulk density) and strongly decelerated. A great portion of the ejecta (even distal ejecta) was not melted and almost all fast ejecta under consideration were not vaporized by the shock wave. In the marine impact, the upper target layer consisted of water. Hence, the water ejecta had the highest velocities, and the solid ejecta (being ejected from deeper target layer) was characterized by lower velocities and, consequently, travelled to smaller distances than in the case of similar subaerial (land) impacts.

To demonstrate this effect further, we carried out numerical simulations in which water layers overlying the sedimentary succession of 200, 400, and 600 m were used (Fig. 6). As expected, the area of ejecta deposition strongly decreases as water depth (H) increases. The water depth, however, does not influence the deposition of close ejecta, since for all depths modelled the curves coincide at a distance below approximately 100 km. The shallower the depth of water, the more extensive the region of coincidence. Note that in deeper water (when water depth is comparable to projectile diameter), the expansion of solid ejecta is restricted by both the walls of the transient water cavity and the water surge. No distal (distance of several crater radii) ejecta occur at all (Shuvalov et al. Forthcoming).

Note that in contrast to subaerial impacts, there are some cases in which marine-target impacts produce solid ejecta with a higher maximum ejection velocity. This increase in ejecta velocity is due to possible differences in the composition of solid targets. Volatile-rich sediments (typical for sea-covered targets) provide a more extensive expansion of shock compressed material than in drier, subaerial materials (O'Keefe et al. 2002). However, this effect dominates only for very shallow water, where sea depth is much less than projectile size (as in the instance of Chicxulub). In our simulations, this effect was taken into account by using equation-of-state for wet sediments (tuff).

Influence of Impact Angle on the Ejecta Formation and Distribution

Although most craters (even those resulting from oblique impacts) are nearly circular, the impact angle can strongly influence ejecta deposition as seen in Pierazzo and Melosh (2000, and references therein). This effect for subaerial impact craters was first demonstrated in experiments by Gault and Wedekind (1978). They found that the ejecta deposits remained near circular for impact angles down to 45°, with only a slight downrange offset of the area of ejecta deposits. As the impact angle decreases below 45°, ejecta deposits become strongly asymmetrical, and the so called "forbidden"

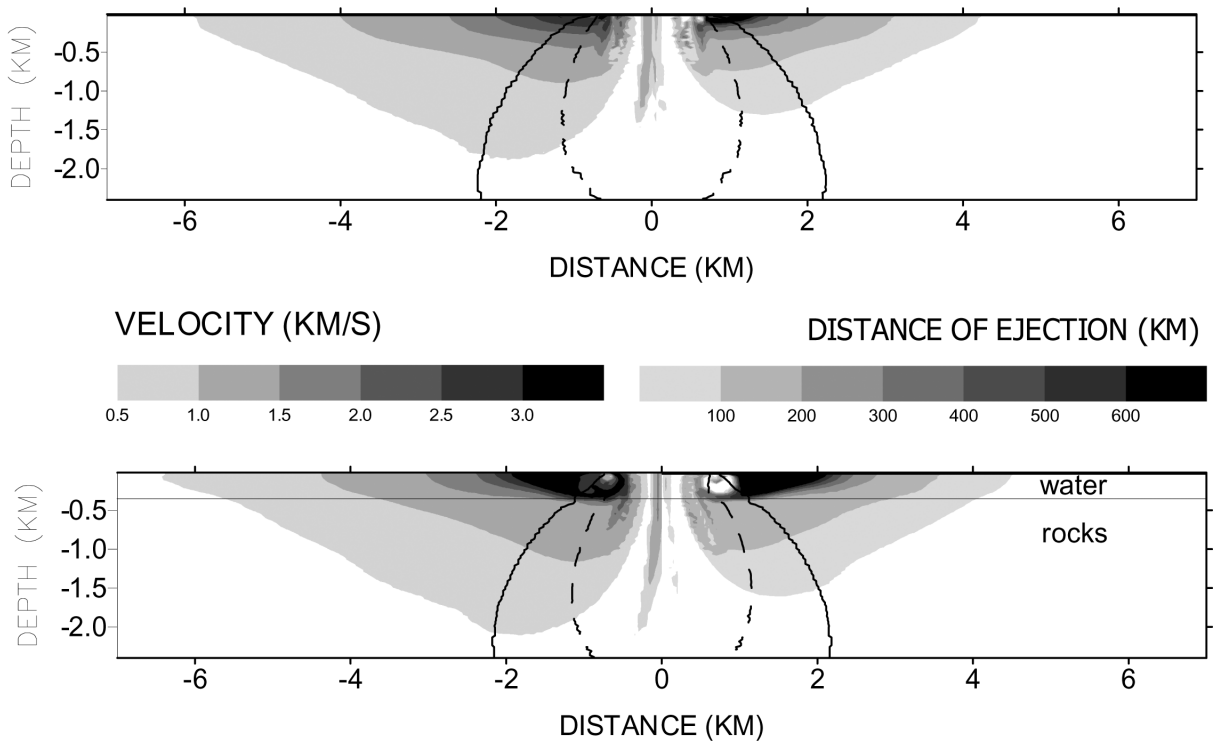

Fig. 5. The left part of each image shows the velocity at which material will be ejected during the impact; the right part shows a distance at which each particular particle will be deposited. The solid/dashed lines delimit the impact melt/vaporization region. The upper image refers to impact on land, the lower one refers to impact into 400 m-deep sea.

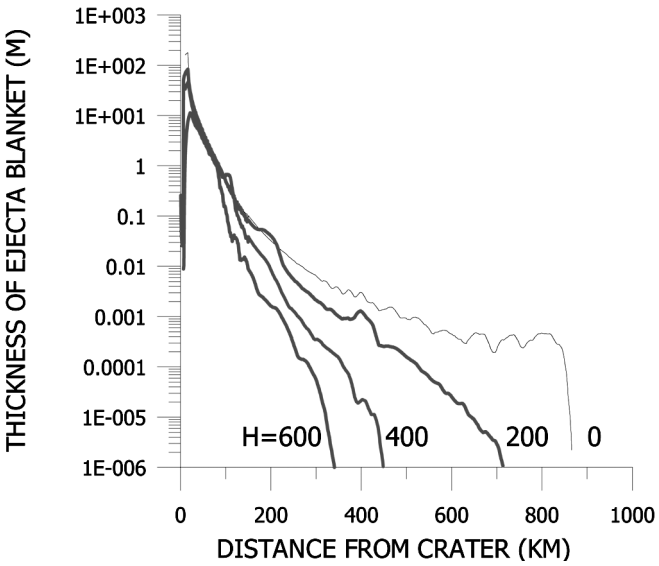

Fig. 6. Thickness of ejecta blanket versus distance from crater center obtained in calculations with t_p = 5 sec, h_{zmax} = 80 m, h_{rmax} = 160 m, and water depth H of 200, 400, and 600 m.

azimuthal zones appear first uprange and then downrange of the crater. Recent experiments by Schultz (1999) show that high-velocity ejecta moves preferably in the downrange direction, while the low velocity ejecta is distributed more evenly around the crater. All these effects were observed on planetary surfaces, each of them containing craters with features characteristic of oblique impacts (Pierazzo and Melosh 2000). Since the paper of Gault and Wedekind (1978) an oblique shape of the ejecta deposits has been considered as the most prominent indicator of oblique impacts.

In order to calculate ejecta deposition after an oblique impact, a 3D version of the model described in the previous sections was used. First, we carried out numerical simulations of vertical and 45° oblique impacts without water to test the performance of the code and to compare results with observational and experimental data. The same 800 m-radius spherical projectile striking the surface at 20 km/s was considered, using a maximum spatial resolution of h_{rmax} = 100 m, and h_{zmax} = 100 m (Figs. 7a and 7b). The initial spatial resolution was 25 m, i.e., 32 cells per projectile radius.

The distribution of ejecta deposits for the vertical impact are in good agreement with those obtained in the 2D simulations, but they strongly differ from the distributions for the oblique impacts. Primarily, the ejecta blanket area strongly increases as impact angle decreases from vertical to 45°. This increase of ejecta blanket is the result of a significant increase in the downrange ejecta velocity. The increase of downrange ejecta velocity was first predicted in numerical simulations by O'Keefe and Ahrens (1986). The central part of the ejecta deposits (at a distance of a few crater radii) looks very similar to experimental data (Fig. 10 of Gault and Wedekind 1978). "Forbidden" azimuthal zones do not

appear either uprange or downrange, although a region of relatively lower thickness of ejecta deposits can be seen downrange at distances above 1000 km (i.e., 25 crater radii) (Fig. 7b). Overall, the decrease in impact angle strongly increases the area of ejecta deposits and makes it strongly asymmetrical, although close ejecta is only slightly asymmetrical (Figs. 7a and 7b).

The ejecta deposits for impacts into 400 m of water at different impact angles substantiate both tendencies emerged so far: a decrease of ejecta deposit area in the presence of water layer and an increase of ejecta deposit area with a decrease of impact angle (Figs. 7c–7e). In the vertical impact of a Mjølnir-like projectile into 400 m of water, the extent of deposits is restricted to within approximately 600 km of the crater. A decrease of impact angle leads to increase of this extent up to 3000–4000 km in the downrange direction, exceeding the ejecta extent from the vertical impact without water, but smaller than the case of oblique impact without water (Fig. 7b). The area of ejecta deposits becomes even more anisotropic than in the equivalent subaerial case. The structure of this downrange zone of deposits probably depends on both water depth and projectile shape. However, these particular distributions illustrate where to look for the deposits: downrange, in the azimuthal zone subtending 60° at a distance less than 3000–4000 km. Note that we neglected the spherical shape of the Earth, which is not very important at distances less than Earth's radius 6300 km.

The projectile ejecta for a 45° impact into the sea (Fig. 7f) have a larger velocity and are even more asymmetrical (distributed over a more narrow angle) than the target ejecta. The projectile decelerates at the left (downrange) wall of crater and gradually moves upward. Five seconds after the impact almost all projectile material is ejected from crater and the crater itself becomes near symmetrical although its center is offset downrange for a distance of ~3 km from the point of initial contact. Due to the high velocity, the projectile ejecta deposits have a local maximum at a distance of ~4000 km, a distance where almost no target ejecta arrive.

Cratering Flow after Oblique Impact

The results presented above show that the ejecta distribution strongly depends on the trajectory angle and for oblique impacts on the proposed direction of projectile motion. The considerable asymmetry of the Mjølnir structure (Tsikalas et al. 1998a; 1998b; 1998c) substantiates an oblique mode of impact. The possibility to determine a value of the trajectory angle, and the direction of the projectile flight for craters resulting from oblique impacts has been discussed in several recent papers. Based on geological and geophysical observations and laboratory experiments, Schultz and Anderson (1996) suggested to derive impact angle and direction from second order asymmetry of impact crater. They applied the following features: 1) maximum amount of central uplift offset in the uprange direction from the geometrical center; 2) breached central-high complex in a direction parallel to the trajectory; 3) large central uplift diameter relative to diameter; 4) larger diameter transverse to the trajectory; 5) maximum structural rim uplift transverse to the trajectory; and 6) shallower than expected excavation. Applying these criteria and detailed geophysical data, Tsikalas (Forthcoming) suggested that Mjølnir crater was formed by an oblique impact coming from south/southwest (SSW) direction at a 45° angle. However, using Magellan data, Ekholm and Melosh (2001) investigated two of these criteria (1 and 3 above, which are frequently used in studies of terrestrial craters). They found that the offset distribution was random and very similar to that of high-angle impacts, and that there was no correlation between the central peak diameter and the impact angle. Numerical modeling can be a good instrument to clarify this problem, allowing one to follow the process of central uplift formation and its evolution in time.

In this section, we consider a 30° and a 45° oblique impact scenario with a Mjølnir-like target. These simulations are much more time-consuming than those described in the previous section because the size of final crater is considerably larger than that of excavation crater, and the time of the modification stage considerably exceeds the time of the excavation stage. For this reason, we used a rather rough grid with h_{rmax} = 320 m, h_{zmax} = 160 m, and neglected the water layer. While using the same solid target, previous simulations (Shuvalov et al. 2002) showed that, in the Mjølnir case, the water layer only slightly influenced the process of crater formation. Ten thousand passive tracer particles were used to follow the displacement of target material and distortion of initially horizontal layers.

Figure 9 shows a sequence of time steps illustrating the 45° impact. Ten seconds after the impact, all projectile material has been ejected from the opening cavity, while the crater reached its maximum depth of about 5 km (approximately 6 km for a vertical impact case, and 4 km for a 30° oblique impact). The central high appears approximately 50 sec after the impact and it is strongly offset in the uprange direction. However, the peak of the central high moves downrange and about 70 sec after impact, it becomes near symmetrical. The central high reaches its maximum height (approximately 1–1.5 km) at about 90 sec, then it slightly descends, and the top portion of its material (highly shocked material lifted from deep layers) spreads along the crater floor. In the final crater (t = 170 sec), the initially 5.5 km layer (shown in Fig. 9 by one black line) is only slightly disturbed, while the target material from a depth of around 4.5 km rises to the surface during the process of central high growth.

The evolution of the transient cavity and selected initially horizontal layers for both variants (30° and 45°) are shown in Fig. 10. In both cases, a point of the rising central high is initially offset in the uprange direction, where the crater reaches its maximum depth. Then, a downrange displacement

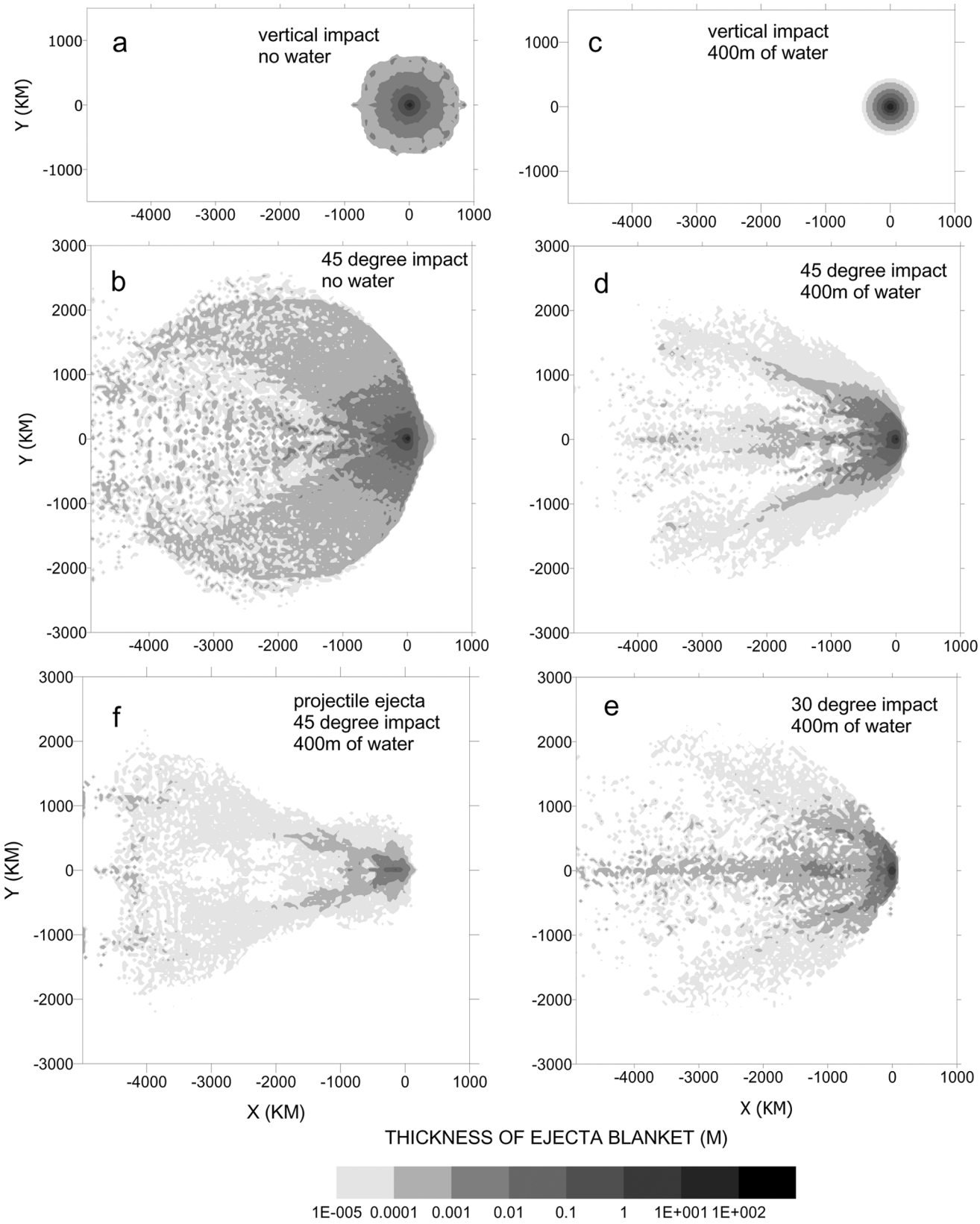

Fig. 7. Distributions of the basement ejecta deposits after the vertical impact without water (a); 45° oblique impact without water (b); vertical impact into 400 m deep sea (c); 45° (d); and 30° oblique impact (e). Plate f shows distribution of projectile material after the 45° oblique impact into the sea 400 m deep. Impact direction is from right to left.

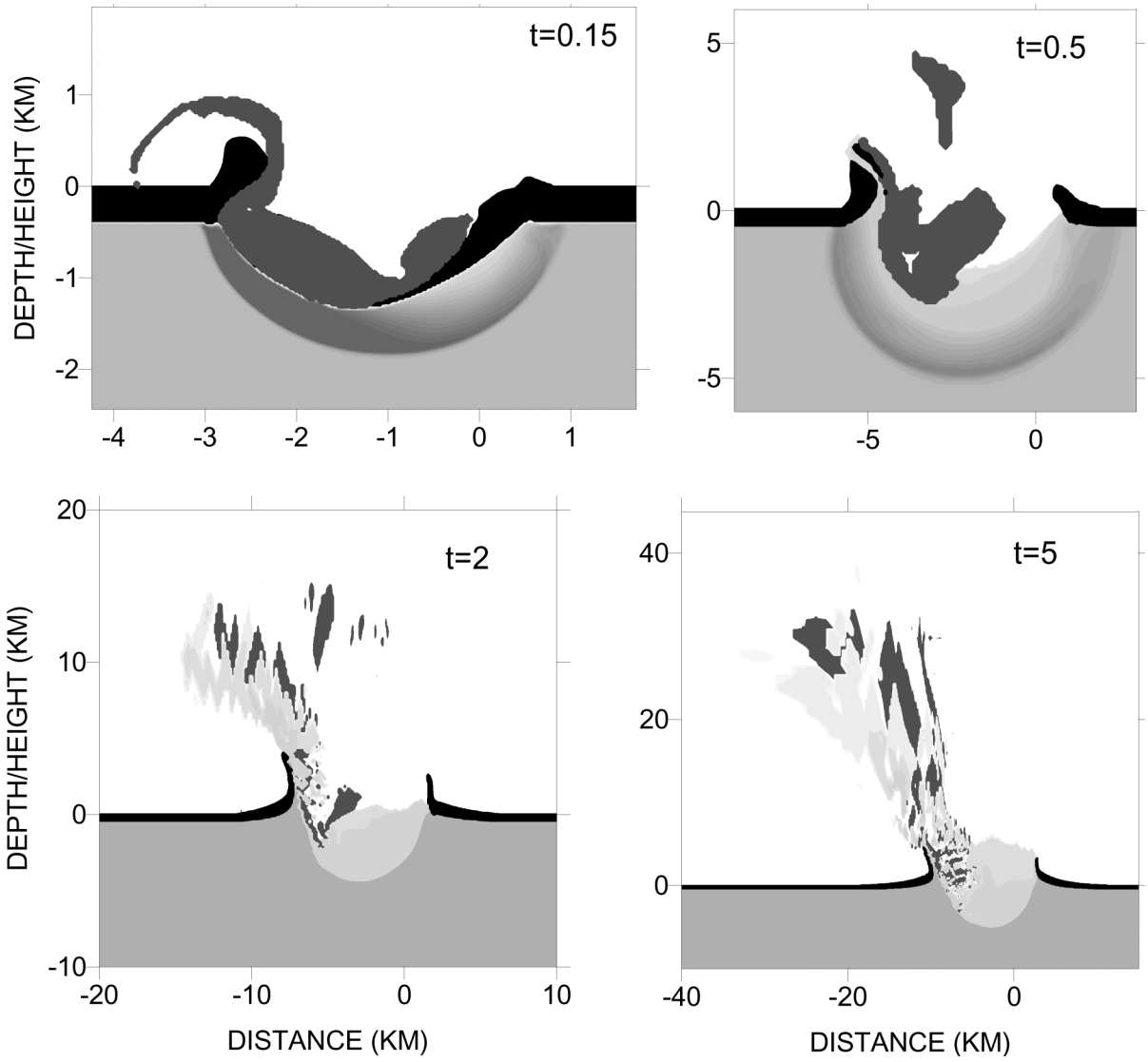

Fig. 8. Initial stage of cratering flow after the 45° oblique impact into the sea 400 m deep. Black shading shows water, dark gray shows projectile material, and light gray (the darker the denser) shows solid target material. Impact direction is from right to left.

of the central high occurs due to: 1) a downrange motion and displacement of central high material; and 2) an increased late rise of the crater floor in the downrange part of the crater (Fig. 10). This downrange directed motion of the central uplift is clearly seen at all depths (see Figs. 10b, 10c, and 10e) and it continues until the central high reaches its maximum height after about 90 sec. Then, the downrange motion practically ends, with the central high even moving slightly uprange (because the rise terminated earlier in the uprange part of the crater, and the downrange slope of the central high was steeper). Fig. 10 also shows the partial spreading of the top level peak material along the crater floor.

The final shape of the two craters are shown in Fig. 11. Unfortunately, our model cannot reproduce rim faults, which normally are considered crater boundaries. Rim faults are the result of local strength fluctuations, while in our model the target is uniform. Furthermore, in the Mjølnir case, the crater rim uplift is very small, and the low spatial resolution of our numerical grid does not allow us to describe it properly. The low rim is most likely a result of a secondary collapse phenomenon. For this reason, to estimate the crater asymmetry, we consider the position of the central high with respect to the ground zero isoline (ground-zero points are shown in Fig. 11 by vertical lines). In both cases, the distance between the central high and downrange and uprange crater boundaries (the ground zero points) is the same within an accuracy of 2–3%. We also considered a position of the central high with respect to the region where shock-induced overpressure exceeds 100 MPa, which is often considered as the strength limit for large rock massifs (isolines are shown in Fig. 11). This comparison does not show any offset between the crater center and central peak. A strong asymmetry (an

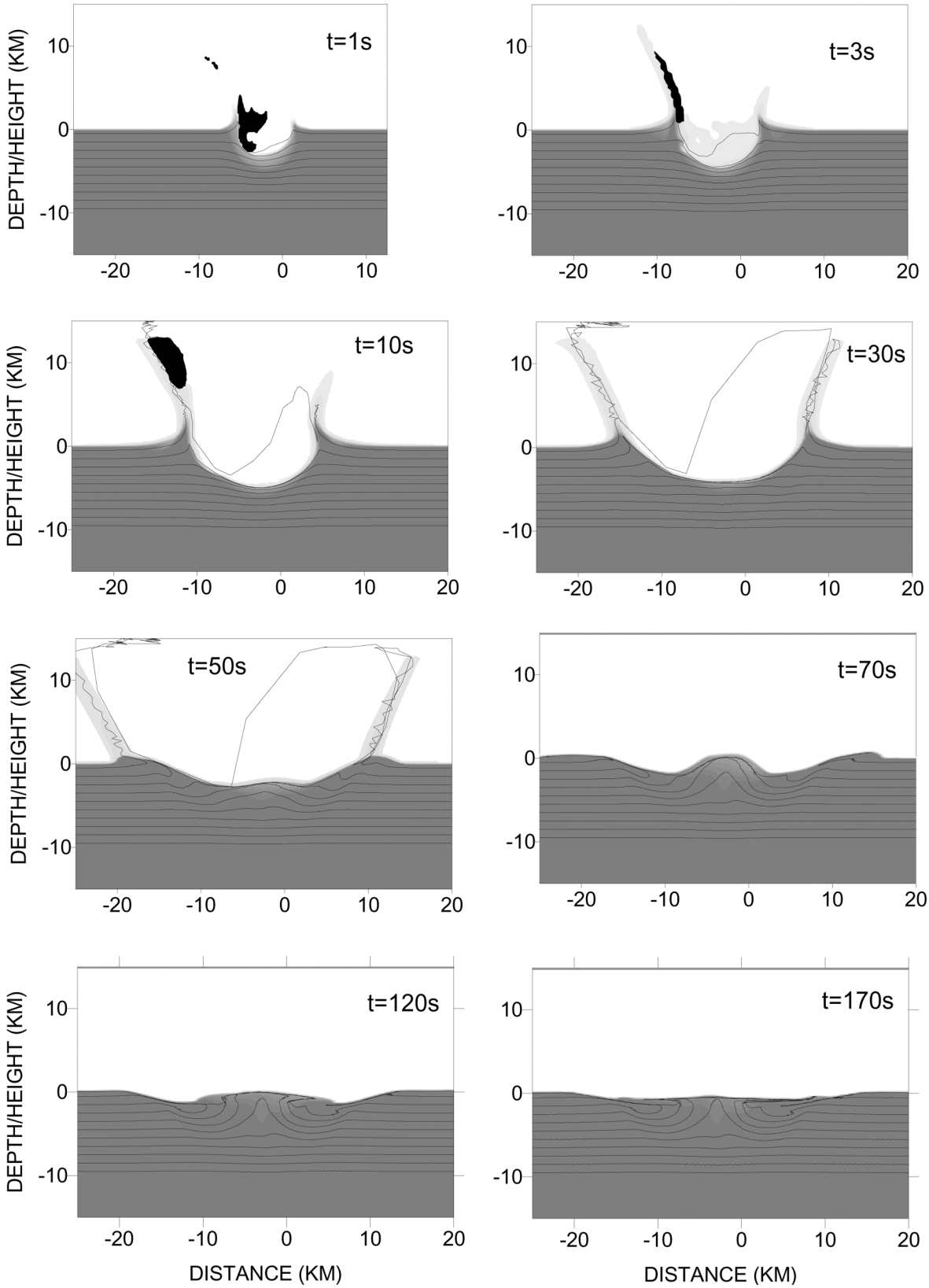

Fig. 9. Evolution of transient carter after the 45° oblique impact. Time steps of 1–170 sec are shown. Black lines show impact induced distortion and displacement of the original horizontal platform layers. Black shading marks projectile material. Gray shading shows target material (the darker the denser). Impact direction is from right to left.

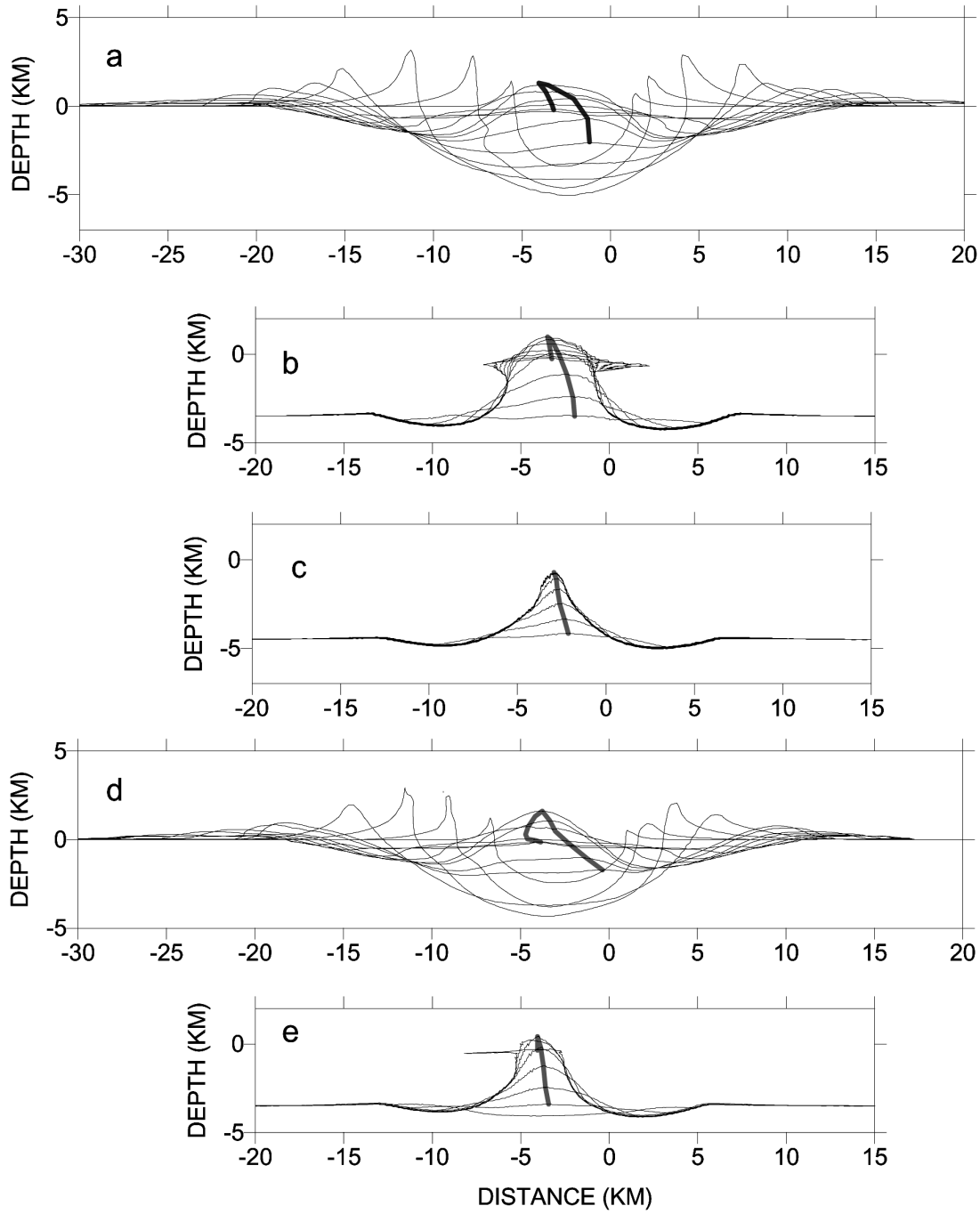

Fig. 10. Evolution of transient cavity and selected original horizontal sedimentary layers. Plates a, b, c refer to 45° impact, plates d, e refer to 30° impact. Thick gray lines show the peak motion. Impact direction is from right to left.

offset between the crater center and central peak) occurs only at the initial stage of central high formation, which took place during a period of about 20 sec, from about 50 sec to about 70 sec after impact.

The shape of the region where the shock-induced overpressure exceeds 3 GPa (i.e., the limiting stress for consolidated rocks) in Fig. 11 (Inner white line) seismically resembles the disturbed region of the Mjølnir crater (Tsikalas et al. 1998b). This region is slightly (~0.5 km) offset uprange. There are some additional faint asymmetrical features: slumping from the crater walls is stronger uprange, strata lines in the central uplift are more concentrated uprange than downrange etc. However, all these effects are very weak and are believed to be comparable to those resulting from local fluctuations in target strength.

In a bird's-eye view, the central high is very close to

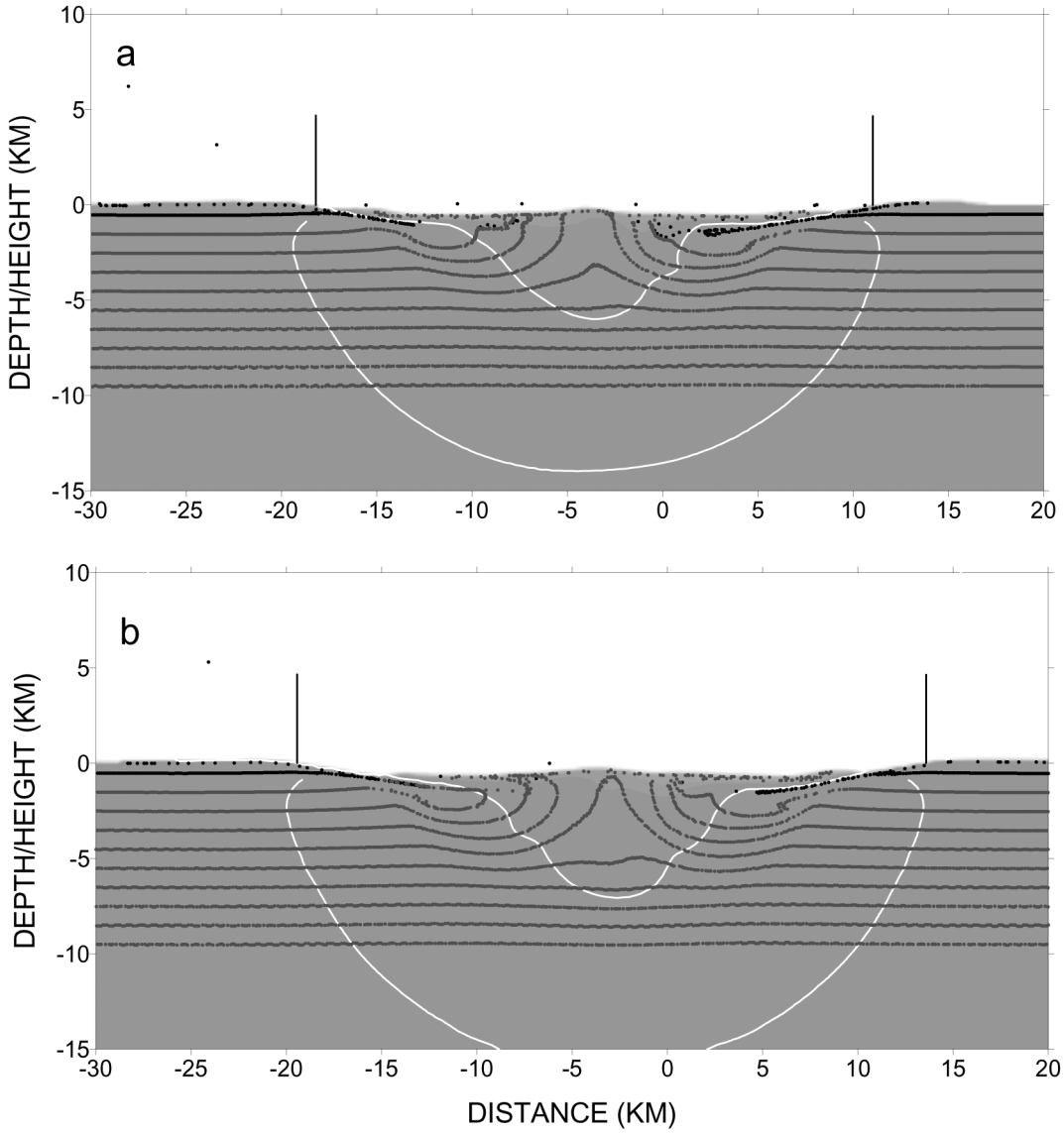

Fig. 11. Final craters for 30° (a) and 45° (b) oblique impacts. White lines show isolines of overpressure corresponding to 100 MPa and 3 GPa. Vertical black lines show zero level points. Black lines show impact induced distortion and displacement of the original horizontal platform layers. Impact direction is from right to left.

geometrical center of the crater (Fig. 12). The crater diameter proves to be slightly elongated along the impact trajectory, contradicting the suggestion of Schultz and Anderson (1996) but in agreement with the geophysical data of Tsikalas (Forthcoming). The elongation along the trajectory can, however, be the result of anisotropical target lithologies.

DISCUSSION AND CONCLUSION

The process of cratering can roughly be divided into three stages: compression/penetration, excavation, and modification (Gault et al. 1968; Melosh 1989). In the case of oblique impacts, the penetration is strongly asymmetrical and occurs with dimensions comparable to projectile size. By contrast, the modification stage is nearly symmetrical because the size of the final crater (i.e., characteristic size of modification process) is considerably larger than the projectile size and initial asymmetry attenuates at this scale. This stage is comparable to a high-energy explosion where shock-wave propagation and cratering depend on the energy release only. The excavation is an intermediate stage with early (fast) ejecta being strongly asymmetrical and late (slow) ejecta (falling near the crater rim) only slightly asymmetrical. Therefore, we can divide all criteria of obliquity for the three groups depending on the governing processes. The distal ejecta are formed at the beginning of the excavation (end of penetration), and the distribution is the most convincing criterion commonly used to determine impact direction on

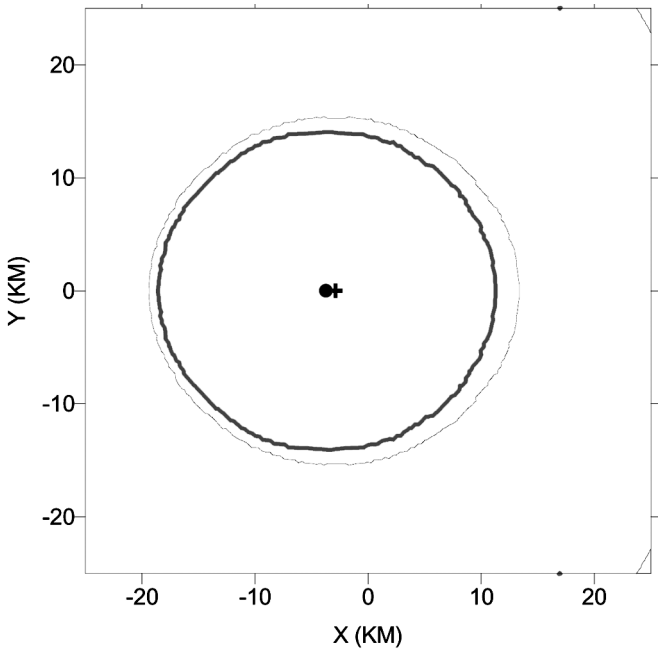

Fig. 12. Final crater shape as it seen from above for 30° (thick gray line) and 45° (thin black line) oblique impacts. Central peak locations are shown by gray circle (30°) and black cross (45°). Impact direction is from right to left.

other planets and satellites. The second group includes the crater rim, which is finally formed at the end of the modification stage. However, the height and width of the rim are determined by a structural uplift and ejecta blanket thickness, which, in turn, are defined by the excavation stage. All other criteria use second order asymmetry features formed during the modification stage (i.e., the most symmetric stage of development). The numerical results support the conclusion of Ekholm and Melosh (2001) that an uprange offset of the central uplift cannot be used as a criterion of obliquity. Moreover, the numerical results are believed to help explain the random distribution of the offset. At the beginning of modification, the transient crater is still asymmetrical and the initial uplift is offset uprange. Thereafter, the uplift moves downrange and then uprange again. The uplift may stop at different points in these quasi-oscillations, depending on target strength, degree of acoustic fluidization, etc. In other words, this effect is comparable to those resulting from average target strength and its local fluctuations. The two simulations presented here (considering a target with special strength) with rather low spatial resolution cannot, of course, give a final solution. The problem needs further investigations, in particular, it is of outmost importance to clarify how the results depend on the target strength (and degree of temporal fluidization) and crater size.

If evaluated more specifically in the case of the Mjølnir impact, it is very important to note that the water level, together with both angle (45°) and direction of impact, controlled the ejecta distribution. With an impact direction from SSW towards NNE (Tsikalas Forthcoming) and the ejecta distribution modeled, the occurrences of Ir enrichments in both the Svalbard and Nordvik sections are likely. It is also clear that searching for distal ejecta southward is less likely to have a positive result (if we accept the preferred SSW to NNE direction). Likewise, we note that the thickness of ejecta may even increase farther away (4000 km) from the crater than the 2500 km Nordvik location of Zakharov et al. (1993). Evidently, such uneven distribution may create some problems in determining the best locations to look for field studies. However, in the Mjølnir case, the secondary redistribution of the returning waters, waves, and currents of the paleo-Barents Sea can level out some of these distributions and reduce the original variations. The skewed evolution of the central high and its possible 0.5–1 km final height illustrate the possible existence of an island in the Barents Sea for several thousand years around the Jurassic/Cretaceous boundary.

The low relief of the Mjølnir crater is clearly a result of the post-impact collapse and modification of the water-saturated marine sediments in the target area. Thus, the skewed development of the central high forecasts more intensive slumping and avalanching in the uprange area of the crater than in the downrange area.

Given these factors, we can only suppose that SSW-NNE direction of the Mjølnir impact suggested by Tsikalas (Forthcoming) is the more probable one because the second order asymmetrical features substantiate this direction.

Acknowledgments–This study was supported by the Norwegian Research Council through Fellowship Program 2002/2003 and also by the Norwegian Science Foundation. The comments of A. Hildebrand, D. King, and E. Pierazzo on an earlier manuscript are highly appreciated.

Editorial Handling—Dr. Elisabetta Pierazzo

REFERENCES

Dienes J. K. and Walsh J. M. 1970. Theory of impact: Some general principles and the method of Eulerian codes. In *High-velocity impact phenomena,* edited by Kinslow R. New York: Academic Press. pp. 46–104.

Dypvik H. and Attrep M., Jr. 1999. Geochemical signals of the late Jurassic marine Mjølnir impact. *Meteoritics & Planetary Science* 34:393–406.

Dypvik H. and Ferrell R. E., Jr. 1998. Clay mineral alteration associated with a meteorite impact in the marine environment (Barents Sea). *Clay Minerals* 33:51–64.

Dypvik H., Gudlaugsson S. T., Tsikalas F., Attrep M., Jr., Ferrell R. E., Jr., Krinsley D. H., Mørk A., Faleide J. I., and Nagy J. 1996. Mjølnir structure: An impact crater in the Barents Sea. *Geology* 24:779–782.

Ekholm A. G. and Melosh J. H. 2001. Crater features diagnostic of oblique impacts: The size and position of the central peak. *Geophysical Research Letters* 28:623–626.

Gault D. E., Quaide W. L., Oberbeck V. R. 1968. Impact cratering mechanics and structures. In *Shock metamorphism of natural*

materials, edited by French B. and Short N. Baltimore: Mono Book Corporation. pp. 87–99.

Gault D. E. and Wedekind J. A. 1978. Experimental studies of oblique impact. Proceedings, 9th Lunar and Planetary Science Conference. pp. 3843–3875.

Gudlaugsson S. T. 1993. Large impact crater in the Barents Sea. *Geology* 21:291–294.

Ivanov B. A. and Turtle E. P. 2001. Modeling impact crater collapse acoustic fluidization implemented into a hydrocode (abstract #1284). Proceedings, 32nd Lunar and Planetary Science Conference.

Lundborg N. 1968. Strength of rock-like materials. *International Journal of Rock Mechanics and Mining Sciences* 5:427–454.

Melosh H. J. 1989. *Impact cratering: A geologic process.* New York: Oxford University Press. 245 p.

Melosh H. J. and Ivanov B. A. 1999. Impact crater collapse. *Annual Review of Earth and Planetary Sciences* 27:385–425.

O'Keefe J. D. and Ahrens T. J. 1986. Oblique impact—A process for obtaining meteorite samples from other planets. *Science* 234: 346–349.

O'Keefe J. D. and Ahrens T. J. 1999. Complex crater: Relationship of stratigraphy and rings to impact conditions. *Journal of Geophysical Research* 104:27091–27104.

O'Keefe J. D., Stewart S. T., and Ahrens T. J. 2002. Impact on comets and asteroids (abstract #2002). Proceedings, 33rd Lunar and Planetary Science Conference.

Pierazzo E. and Melosh H. J. 2000. Understanding oblique impacts from experiments, observations, and modeling. *Annual Review of Earth and Planetary Sciences* 28:141–167.

Robin E., Rocchia R., Siret D., and Dypvik H. 2001. Discovery of nickel-iron oxide particles in the ejecta-bearing stratia of the latest Jurassic Mjølnir meteorite impact (Barents Sea). In *Submarine Craters and Ejecta Crater correlation* (NGF Abstracts and Proceedings), edited by Smelror M., Dypvik H. and Tsikalas F. Trondheim: Tapir Academic Press. pp. 67–68.

Schultz P. H. 1999. Ejecta distributions from oblique impacts into particulate targets. (abstract #1919). Proceedings, 30th Lunar and Planetary Science Conference.

Schultz P. H. and Anderson R. R. 1996. Asymmetry of the Manson impact structure: Evidence for impact angle and direction. In *The Manson impact structure, Iowa: Anatomy of an impact crater.* Special Paper 302. Washington D.C.: Geological Society of America. pp. 397–417.

Schultz P. H. and Gault D. E. 1982. Impact ejecta dynamics in an atmosphere: Experimental results and extrapolations. In *Geological implications of impacts of large asteroids and comets on the Earth,* edited by Silver L. T. and Schultz P. H. Special Paper 190. Washington D.C.: Geological Society of America. pp. 153–174.

Shuvalov V. V. 1999. Multi-dimensional hydrodynamic code SOVA for interfacial flows: Application to thermal layer effect. *Shock Waves* 9:381–390.

Shuvalov V. V. 2002. Displacement of target material due to impact. (abstract #1259). Proceedings, 33rd Lunar and Planetary Science Conference.

Shuvalov V. V., Dypvik H., and Tsikalas F. 2002. Numerical simulations of the Mjølnir marine impact crater. *Journal of Geophysical Research* 107, doi: 10.1029/2001JE001698.

Shuvalov V., Ormö J., and Lindström M. Forthcoming. Hydrocode simulation of the Lockne marine target impact event. In *Impact tectonism,* edited by Koeberl C. and Henkel H. Heidelberg: Springer Verlag.

Smelror M., Kelly R. A., Dypvik H., Mørk A., Nagy J., and Tsikalas F. 2001. Mjølnir (Barents Sea) meteorite impact ejecta offers a Volgian-Ryazanian boundary marker. *Newletter on Stratigraphy* 38:129–140.

Thompson S. L. and Lauson H. S. 1972. *Improvements in the Chart D radiation-hydrodynamic CODE III: Revised analytic equations of state.* Report SC-RR-71 0714. Albuquerque: Sandia National Laboratory. 119 p.

Tillotson J. H. 1962. Metallic equations of state for hypervelocity impact. General Atomic Report GA-3216. 137 p.

Tsikalas F. Forthcoming. Mjølnir structure as a result of oblique impact: Asymmetry evidence constrains impact direction and angle. In *Impact tectonism,* edited by Koeberl C. and Henkel H. Heidelberg: Springer Verlag.

Tsikalas F., Gudlaugsson S. T., and Faleide J. I. 1998a. The anatomy of a buried complex impact structure: The Mjølnir structure, Barents Sea. *Journal of Geophysical Research* 103:30469–30484.

Tsikalas F., Gudlaugsson S. T., and Faleide J. I. 1998b. Collapse, infilling, and postimpact deformation at the Mjølnir impact crater, Barents Sea. Bulletin 110. Washington D.C.: Geological Society of America.

Tsikalas F. S., Gudlaugsson S. T., and Faleide J. I. 1998c. Integrated geophysical analysis supporting the impact origin of the Mjølnir structure, Barents Sea. *Tectonophysics* 289:257–280.

Zakharov V. A., Lapukhov A. S., and Shenfil O. V. 1993. Iridium anomaly at the Jurassic-Cretaceous boundary in northern Siberia. *Russian Geology and Geophysics* 34:83–90.

Zamyshliaev B. V. and Evterev L. S. 1990. *Models of dynamic deforming and failure for ground media.* Moscow: Nauka Press. 215 p. In Russian.